

Supplement of Atmos. Chem. Phys., 14, 11031–11063, 2014
<http://www.atmos-chem-phys.net/14/11031/2014/>
doi:10.5194/acp-14-11031-2014-supplement
© Author(s) 2014. CC Attribution 3.0 License.



Supplement of

A global model simulation of present and future nitrate aerosols and their direct radiative forcing of climate

D. A. Hauglustaine et al.

Correspondence to: D. A. Hauglustaine (didier.hauglustaine@lsce.ipsl.fr)

8 **Model description**

9 Free ammonia is used for the neutralization of nitric acid to ammonium nitrate aerosol
10 following the equilibrium reaction:



12 The equilibrium constant (K_p) of (1) strongly depends on relative humidity and temperature.
13 The parameterization used for this dependence is based on Mozurkewich (1993). First, the
14 deliquescence relative humidity (DRH, %) is calculated based on Seinfeld and Pandis (1998):

$$15 \quad \text{DRH} = \exp(723.7/T + 1.6954) \quad (2)$$

16 where T is the air temperature (K). For relative humidities lower than DRH, $K_p = K_{pd}$ and is
17 calculated with:

$$18 \quad K_{pd} = \exp[118.87 - 24084/T - 6.025 \ln(T)] \quad (3)$$

19 For relative humidities higher than DRH, $K_p = K_{ph}$ and depends on both temperature and
20 relative humidity (RH) and is calculated based on :

$$21 \quad K_{ph} = K_{pd} (p_1 - p_2 \text{RH}_1 + p_3 \text{RH}_1^2) \text{RH}_1^{1.75} \quad (4)$$

22 With RH_1 defined as $(1 - \text{RH}/100)$ and p_1 , p_2 , and p_3 provided by:

$$23 \quad p_1 = \exp[-135.94 + 8763/T + 19.12 \ln(T)] \quad (5)$$

$$24 \quad p_2 = \exp[-122.65 + 9969/T + 16.22 \ln(T)] \quad (6)$$

$$25 \quad p_3 = \exp[-182.61 + 13875/T + 24.46 \ln(T)] \quad (7)$$

26

27 **Model evaluation**

28 **Box model simulations**

29 In order to evaluate the thermodynamic nitrate aerosol module developed and used in INCA,
30 we have developed a box model version and used it as a stand-alone version to be evaluated
31 against the ISORROPIA version 2.1 reference model (Nenes et al., 1998). Both the INCA box
32 model and ISORROPIA are constrained by the same input parameters. The input parameters
33 are then varied in order to compare the behavior of the two models across the range of

34 variation in key inputs (i.e., total sulfate TS, total ammonia TA, total nitrate TN, relative
35 humidity RH, and temperature T). The reference input parameters for all simulations are : T =
36 280K, RH = 0.9, TS = 2 $\mu\text{g}/\text{m}^3$, TA = 4 $\mu\text{g}/\text{m}^3$, and TN= 5 $\mu\text{g}/\text{m}^3$. Figure S1 shows the
37 evolution of the simulated NO_3^- and NH_4^+ equilibrium concentrations when these parameters
38 are varied separately over a given interval and compares the output to the ISORROPIA
39 results. Overall an excellent agreement is obtained between the INCA module and
40 ISORROPIA. The sensitivity of the two models to key environmental parameters as
41 encountered in the global atmosphere are very similar and the simulated concentrations in
42 close agreement. The major disagreement we note is at sulfate concentrations larger than
43 about 10 $\mu\text{g}/\text{m}^3$ for which the INCA module forms ammonium sulfate preferentially and
44 hence significantly underestimates the ammonium nitrate levels compared to ISORROPIA.
45 This disagreement has no effect on the simulated global concentrations since sulfate
46 concentrations larger than 10 $\mu\text{g}/\text{m}^3$ are hardly not reached in the global model grid-cells. It
47 should also be pointed out that at temperature higher than about 295K, the volatilization of
48 ammonium nitrate is too efficient and the concentration simulated with INCA drops more
49 rapidly to zero than in ISORROPIA. This limitation has to be kept in mind but even under a
50 warming climate these high temperatures are not often reached in regions with fine particulate
51 nitrate formation or only occasionally and will have a minor impact on the model results.

52 **Diurnal variations**

53 Nitrate aerosols have the ability to evaporate back into the gas phase. As illustrated by high
54 temporal resolution measurements (e.g., Slanina et al., 2001; Trebs et al., 2004; ten Brink et
55 al., 2007; Dall'Osto et al., 2009; Morgan et al., 2010; Schaap et al., 2011; Mensah et al., 2012;
56 Aan de Brugh et al., 2012), this means that nitrates have a pronounced diurnal cycle and
57 spend most of the daytime in the gas phase. The detailed evaluation of the diurnal cycle is out
58 of the scope of the use of a global model and of this paper. However, since this diurnal
59 variation has an impact on the radiative forcing, we illustrate in Figure S2 the simulated
60 diurnal variation of nitrate concentrations at four different sites for the period 1/8/2009 to
61 30/10/2009. A very pronounced diurnal cycle is indeed calculated over the Po Valley or over
62 China. As measured at several sites by the studies mentioned above, nitrates build up during
63 the night and reach a maximum concentration early in the morning. The minimum in NO_3^-
64 concentrations occur during daytime due to increased boundary layer height and increased
65 instability at higher temperature, and are often close to zero during that period. This daytime
66 minimum coincides with a maximum in HNO_3 concentrations (not shown) suggesting that

67 volatilization of nitrate particles indeed occurs as illustrated by several studies (e.g., Dall'Osto
68 et al., 2009; Schaap et al., 2011; Aan de Brugh et al., 2012) . In England, the nitrate
69 concentrations and their variation are in agreement with the range of about 0-12 $\mu\text{g}/\text{m}^3$ and
70 variability measured by Dall'Osto et al. (2009) in October 2006. The variability of NO_3 in the
71 model can be explained by a combination of the diurnal cycle associated with the
72 thermodynamic equilibrium of nitrate formation, superimposed on a variability associated
73 with changing meteorological conditions and transport of pollution episodes from the
74 continent. High pollution episodes of nitrate particles are also simulated in the Netherlands
75 where NH_3 concentrations reach more than 10 $\mu\text{g}/\text{m}^3$.

76 **Present-day nitrate column**

77 Figure S3 shows the three components of the total nitrate column and shows the fine mode,
78 coarse mode on dust and coarse mode on sea-salt separately. This figure clearly shows that
79 fine nitrate particles associated with anthropogenic emissions contribute to a large extent to
80 the maximum calculated in the central US, in Northern Europe and over the Po Valley, in
81 Northern India and in China. Over Africa, Saudi Arabia, Central Europe and in Northern
82 China, nitrates on dust contribute for more than 4-10 mg/m^2 to the nitrate column. Over the
83 Mediterranean and in Southern Europe, the contribution of coarse nitrates on dust represents
84 about 50% of the calculated total nitrate column. The contribution of nitrates on sea-salt is
85 lower and generally close to 0.5 mg/m^2 over the continents. It only reaches 1 mg/m^2 in
86 localized areas, in particular off the coast of the Eastern US, or over the Mediterranean where
87 both pollution and sea-salt particle are present.

88 **Comparison with measurements**

89 Figure S4-S6 compare the simulated and measured surface concentrations of SO_4^- , NH_4^+ , and
90 NO_3^- from the EBAS database at NILU. EBAS holds data from EMEP (emep.int), from the
91 US National Atmospheric Deposition Program/National Trend Network (NADP/NTN;
92 <http://nadp.sws.uiuc.edu/NTN>), from the US Inter- agency Monitoring of Protected Visual
93 Environments (IMPROVE; <http://vista.cira.colostate.edu/IMPROVE>), from the Clean Air
94 Status and Trends Network (CASTNET; <http://java.epa.gov/castnet>) and the EANET, Data
95 on the Acid Deposition in the East Asian Region (<http://www.eanet.cc/>). These comparisons
96 have been prepared using the AEROCOM evaluation tools (Schulz et al., 2006). The aerosols
97 measurements are mostly from the CASTNET/IMPROVE network over Northern America,

98 from the EMEP network in Europe. This evaluation is performed for the year 2006 based on
99 matching daily mean data, averaged to monthly means.

100 To obtain a large spatial coverage with respect to evaluation of nitrate and ammonium model
101 values we have included measurements from different methods. These use different
102 combinations of filterpacks and denuders. Little harmonization of the methods has been
103 achieved globally and it is not possible to rely on just one method. Depending on filter type,
104 sampling set-up, temperature and changing ambient conditions during a sampling interval
105 considerable sampling artefacts may occur. At higher temperatures, evaporation of
106 ammonium nitrate from filters has been shown to lead to losses of up to 50% in summer
107 conditions (Vecchi et al., 2009; Sickles and Shadwick, 2002; Allegrini et al., 1994; Yu et al.,
108 2005, Hering and Cass, 1999; Chow et al., 2005, Ashbaugh and Elfred, 2004, Schaap et al.,
109 2004, Schaap et al., 2002). Such sampling artefacts may explain in total a positive model bias,
110 while negative model bias clearly points to model errors. We do not find a clear north-south
111 gradient in bias, neither in Europe nor in Northern America, higher temperatures in the south
112 are not associated with higher positive model bias. However, in central Europe there are
113 several sites, where the positive bias of the model is high in summer and almost absent in
114 winter. In depth inspection of nitrate bias on a map and per measurement site may be accessed
115 via the AeroCom web interface ([http://aerocom.met.no/cgi-](http://aerocom.met.no/cgi-bin/aerocom/surfobs_annualrs.pl?PROJECT=INCA)
116 [bin/aerocom/surfobs_annualrs.pl?PROJECT=INCA](http://aerocom.met.no/cgi-bin/aerocom/surfobs_annualrs.pl?PROJECT=INCA)
117 [&Run0=LOI_DH10n&Parameter0=SCONC_NO3](http://aerocom.met.no/cgi-bin/aerocom/surfobs_annualrs.pl?PROJECT=INCA)).

118 Figure S7-S10 compares the wet deposition of SO_x ($=\text{SO}_2+\text{SO}_4^-$), NH_x ($=\text{NH}_3+\text{NH}_4^+$), and
119 NO_y ($=\text{NO}+\text{NO}_2+\text{NO}_3+\text{HNO}_2+\text{HNO}_3+\text{HNO}_4+2\text{N}_2\text{O}_5+\text{PAN}+\text{organic nitrates}+\text{particulate NO}_3^-$
120) calculated by the model with the measurements from the EMEP network over Europe, from
121 the NADP network over Northern America and from the EANET network over Eastern Asia.
122 Over the whole dataset, the sulfate deposition is underestimated by the model with a
123 Normalized Mean Bias (NMB) of -59%, mostly driven by a high underestimation over
124 Eastern Asia. Over Europe the deposition is slightly underestimated by the model by 27% and
125 by 20% in Northern America. In Eastern Asia, a higher underestimation of 80% is obtained.
126 The wet deposition of NH_x is underestimated by 34% in the model over the whole dataset.
127 This term is well represented in Europe (NMB=-4.5%) and to a lesser extent in Northern
128 America (NMB=-32%). This deposition term is again significantly underestimated in Eastern
129 Asia (NMB=-60%). The wet deposition of oxidized nitrogen from $\text{HNO}_3+\text{NO}_3^-$ is
130 underestimated by 40% over the whole domain. This deposition term is relatively well

131 represented in Europe but underestimated by -28% and better represented over Northern
132 America (NMB=+13%). Again, in Eastern Asia, a significant underestimate of the wet
133 deposition is obtained (NMB=-54%).

134

135

136 Figure S11 present an evaluation of the calculated total AOD by comparing with the
137 measurements from the AERONET network (Holben et al., 2001, Kinne et al., 2006).
138 Matching daily data from the model and Aeronet were aggregated to monthly averages.
139 Worldwide, the measured and modeled AOD show a relatively good correlation (R=0.57).
140 The arithmetic mean for the measurements of 0.226 is however underestimated by the
141 modeled values of 0.202 with a Normalized Mean Bias (NMB) of -11%. A good agreement
142 with the AERONET measurements is obtained over Northern America. Over this region the
143 model slightly underestimates the measurements (NMB=-4.5%, R=0.77). Over Africa, higher
144 AOD associated with dust aerosols are calculated. A fairly good correlation is reached
145 (R=0.66) with also a light underestimate by the model of -10%. Over Eastern Asia, the model
146 underestimate the AOD (NMB=-39%). Over Europe, the model slightly overestimates the
147 measurements (NMB=+6%).

148 **Future evolution of atmospheric composition and surface deposition**

149 Figure S12 shows the change in NH₃ surface concentration from the present-day levels in
150 2030 and 2100 for both RCP4.5 and RCP8.5 (see Fig. 6 from the manuscript for the reference
151 level). For RCP8.5 a significant increase is calculated everywhere in 2030 and 2100 except in
152 Indonesia where biomass burning emissions are reduced. In the central United States,
153 Northern and central Europe, India and China, NH₃ increases by up to 2 µg/m³ in 2100. For
154 the RCP4.5 scenario, a significant increase is still predicted in India and in China where
155 emissions are still predicted to rise. However, concentrations are significantly reduced in
156 Western and Eastern Europe by up to 1 µg/m³ and a lesser increase of 0.5-1 µg/m³ is
157 calculated in the central US. Figure S13 shows the corresponding change in HNO₃ surface
158 concentrations. Due to a reduction in NO_x emissions, HNO₃ has already significantly
159 decreased in 2030 in Northern America and Europe in both scenarios. In contrast, a strong
160 increase is calculated in India and in China reaching more than 2 µg/m³ in 2030. In 2100, the
161 HNO₃ reduction is almost generalized over the continents with the exception of biomass

162 burning regions in Africa and India in the case of RCP8.5. Figure S14 shows the change in
163 SO_4^{2-} surface concentration in 2030 and 2100 for both RCP8.5 and RCP4.5. The concentration
164 increases in India and Southeast Asia by more than $2 \mu\text{g}/\text{m}^3$ in 2030. As expected from the
165 sharp decrease in SO_2 emissions, at the end of the XXIst century, a general decrease of the
166 surface concentration is calculated, reaching more than $2 \mu\text{g}/\text{m}^3$ in Northern America, Europe,
167 and China. As a result of these changes in nitrate precursor surface concentrations, nitrate
168 particles are expected to undergo significant variations in the future. Figure S15, shows the
169 evolution of nitrate particles surface concentrations for 2030 and 2100 and for scenarios
170 RCP8.5 and RCP4.5. The surface concentration increases in India and Southeast Asia by
171 more than $2 \mu\text{g}/\text{m}^3$ in 2030. As a consequence of the sharp decrease in HNO_3 concentrations, a
172 decrease of the surface concentration is calculated, reaching more than $2 \mu\text{g}/\text{m}^3$ in Northern
173 America and Europe in 2030 and 2100. This decrease in surface nitrate concentrations also
174 occurs in China in 2100.

175 Figure S16, shows the change from the present-day (see Fig. 4 from the main paper for
176 reference levels) of the nitrate column in 2030 and 2100 for the two extremes scenarios
177 RCP4.5 and RCP8.5. The change in nitrate precursors is responsible for a strong increase of
178 the nitrate column in the northern hemisphere. The strong decrease in nitrate surface
179 concentrations calculated over Europe and China in 2030 and 2100 dominates the change in
180 the column which decreases by up to $2 \text{mg}/\text{m}^2$ over these regions.

181 Figure S17 shows the evolution of the total nitrogen deposition averaged over various regions
182 of the world. The total $\text{NO}_y + \text{NH}_x$ (wet + dry) deposition is presented. In Europe and
183 Northern America, the total N deposition slightly decreases or remains close to its present-day
184 value in the case of scenario RCP8.5. In Asia and India, the NO_y deposition generally
185 increases in 2030 or 2050 due to higher NO_x emissions in these regions before decreasing at
186 the end of the XXIst century. In addition, the NH_x deposition generally increases during the
187 course of the century to reach maximum values in 2100. Figure S18 shows that the fraction of
188 N deposited as NH_x increases from about 60% to 80% in these regions. The same tendency is
189 found over oceanic regions and globally. The total N deposited remains fairly stable or
190 slightly decreases in these regions during the XXIst century but the fraction of N deposited as
191 NH_x increases from 45% to 55-70% over the ocean and from 55% to 70-80% globally.

192

193 **References**

- 194 Aan de Brugh, J. M. J., J. S. Henzing, M. Schaap, W. T. Morgan, C. C. van Heerwaarden, E.
195 P. Weijers, H. Coe, and M. C. Krol, Modelling the partitioning of ammonium nitrate in the
196 convective boundary layer, *Atmos. Chem. Phys.*, 12, 3005-3023, 2012.
- 197 Allegrini, I., A. Febo, C. Perrino and P. Masia, Measurement of Atmospheric Nitric-Acid in
198 Gas-Phase and Nitrate in Particulate Matter by Means of Annular Denuders, *International*
199 *Journal of Environmental Analytical Chemistry*, 54, 183-201, 1994.
- 200 Ashbaugh, L. L. and R. A. Eldred, Loss of Particle Nitrate from Teflon Sampling Filters:
201 Effects on Measured Gravimetric Mass in California and in the Improve Network, *Journal of*
202 *the Air & Waste Management Association*, 54, 93-104, 2004.
- 203 Chow, J. C., J. G. Watson, D. H. Lowenthal and K. L. Magliano, Loss of Pm_{2.5} Nitrate from
204 Filter Samples in Central California, *Journal of the Air & Waste Management Association*
205 55, 1158-1168, 2005.
- 206 Dall'Osto, M., R. M. Harrison, H. Coe, P. I. Williams, and J. D. Allan, Real time chemical
207 characterization of local and regional nitrate aerosols, *Atmos. Chem. Phys.*, 9, 3709-3720,
208 2009.
- 209 Hering, S. and G. Cass, The Magnitude of Bias in the Measurement of Pm_{2.5} Arising from
210 Volatilization of Particulate Nitrate from Teflon Filters, *Journal of the Air & Waste*
211 *Management Association*, 49, 725-733, 1999.
- 212 Mensah, A. A., R. Holzinger, R. Otjes, A. Trimborn, Th. F. Mentel, H. ten Brink, B. Hensing,
213 and A. Kiendler-Scharr, Aerosol chemical composition at Cabauw, the Netherlands as
214 observed in two intensive periods in May 2008 and March 2009, *Atmos. Chem. Phys.*, 12,
215 4723-4742, 2012.
- 216 Morgan, W. T., J. D. Allan, K. N. Bower, M. Esselborn, B. Harris, J. S. Henzing, E. J.
217 Highwood, A. Kiendler-Scharr, G. R. McMeeking, A. A. Mensah, M. J. Northway, S.
218 Osborne, P. I. Williams, R. Krejci, and H. Coe, Enhancement of the aerosol direct radiative
219 effect by semi-volatile aerosol components: airborne measurements in North-Western Europe,
220 *Atmos. Chem. Phys.*, 10, 8151-8171, 2010.

221 Mozurkewich, M., The dissociation constant of ammonium nitrate and its dependence on
222 temperature, relative humidity and particle size, *Atmos. Environ.*, 27A, 261-270, 1993.

223 Nenes, A., S. Pandis, and C. Pilinis, ISORROPIA: a new thermodynamic equilibrium model
224 for multiphase multicomponent inorganic aerosols, *Aquat. Geochem.*, 4, 123-152, 1998.

225 Schaap, M., K. Muller and H. M. ten Brink, Constructing the European Aerosol Nitrate
226 Concentration Field from Quality Analysed Data, *Atmospheric Environment*, 36, 1323-1335,
227 2002.

228 Schaap, M., G. Spindler, M. Schulz, K. Acker, W. Maenhaut, A. Berner, W. Wieprecht, N.
229 Streit, K. Muller, E. Brüggemann, X. Chi, J. P. Putaud, R. Hitzinger, H. Puxbaum, U.
230 Baltensperger and H. ten Brink, Artefacts in the Sampling of Nitrate Studied in the Intercomp
231 Campaigns of Eurotrac-Aerosol, *Atmospheric Environment*, 38, 6487-6496, 2004.

232 Schaap, M., R. P. Otjes, and E. P. Weijers, Illustrating the benefit of using hourly monitoring
233 data on secondary inorganic aerosol and its precursors for model evaluation, *Atmos. Chem.*
234 *Phys.*, 11, 11041-11053, 2011.

235 Seinfeld, J. H., and S. N. Pandis, *Atmospheric chemistry and Physics*, John Wiley and Sons,
236 New York, 1998.

237 Sickles, J. E. and D. S. Shadwick, Biases in Clean Air Status and Trends Network Filter Pack
238 Results Associated with Sampling Protocol, *Atmospheric Environment*, 36, 4687-4698, 2002.

239 Slanina, J., H. M. ten Brink, R. P. Otjes, A. Even, P. Jongejan, A. Khlystov, A. Waijers-
240 Ijpelaan, M. Hu, and Y. Lu, The continuous analysis of nitrate and ammonium in aerosols by
241 the steam jet aerosol collector (SJAC): extension and validation of the methodology, *Atmos.*
242 *Environ.*, 35, 2319-2330, 2001.

243 Ten Brink, H., R. Otjes, P. Jongejan, S. Slanina, An instrument for semi-continuous
244 monitoring of the size-distribution of nitrate, ammonium, sulphate and chloride in aerosol,
245 *Atmos. Environ.*, 41, 2768-2779, 2007.

246 Trebs, I., F. X. Meixner, J. Slanina, R. Otjes, P. Jongejan, and M. O. Andreae, Real-time
247 measurements of ammonia, acidic trace gases and water-soluble inorganic aerosol species at a
248 rural site in the Amazon Basin, *Atmos. Chem. Phys.*, 4, 967-987, 2004.

249 Vecchi, R., G. Valli, P. Fermo, A. D'Alessandro, A. Piazzalunga and V. Bernardoni, Organic
250 and Inorganic Sampling Artefacts Assessment, *Atmospheric Environment*, 43, 1713-1720,
251 2009.

252 Yu, X. Y., L. Taehyoung, B. Ayres, S. M. Kreidenweis, J. L. Collett and W. Maim.
253 Particulate Nitrate Measurement Using Nylon Filters, *Journal of the Air & Waste*
254 *Management Association*, 55, 1100-1110, 2005.

255

256 **Figure Captions**

257

258 Figure S1. Variation of NO_3^- (blue) and NH_4^+ (red) equilibrium concentrations ($\mu\text{g}/\text{m}^3$) as a
259 function of total sulfate, total ammonia, total nitrate ($\mu\text{g}/\text{m}^3$), relative humidity (%) and
260 temperature (T). INCA model results : solid line, ISORROPIA model: triangles.

261

262 Figure S2. Simulated diurnal variation of NO_3^- surface concentration ($\mu\text{g}/\text{m}^3$) during the
263 1/08/2009 to 30/10/2009 period in England, the Po valley, The Netherlands, and in Northern
264 China.

265

266 Figure S3. Annual mean tropospheric column of (top) fine mode nitrate aerosols, (middle)
267 coarse mode nitrates on dust, and (bottom) coarse mode nitrates on sea-salt simulated for
268 present-day conditions (mg/m^2).

269

270 Figure S4. Simulated surface concentration of sulfates ($\mu\text{S}/\text{m}^3$), ammonium ($\mu\text{N}/\text{m}^3$), and
271 nitrates ($\mu\text{N}/\text{m}^3$) for the year 2006 compared to EBAS data over the world (all available data).
272 Dashed lines indicate 1:2 and 2:1 ratios.

273

274 Figure S5. Simulated surface concentration of sulfates ($\mu\text{S}/\text{m}^3$), ammonium ($\mu\text{N}/\text{m}^3$), and
275 nitrates ($\mu\text{N}/\text{m}^3$) for the year 2006 compared to EBAS data over Europe. Dashed lines indicate
276 1:2 and 2:1 ratios.

277

278 Figure S6. Simulated surface concentration of sulfates ($\mu\text{S}/\text{m}^3$), ammonium ($\mu\text{N}/\text{m}^3$), and
279 nitrates ($\mu\text{N}/\text{m}^3$) for the year 2006 compared to EBAS data over Northern America. Dashed
280 lines indicate 1:2 and 2:1 ratios.

281

282 Figure S7. Simulated SO_x ($\text{gS}/\text{m}^2/\text{yr}$), NH_x and NO_y ($\text{gN}/\text{m}^2/\text{yr}$) wet deposition for the year
283 2006 compared to EBAS data for the world (all available data). Dashed lines indicate 1:2 and
284 2:1 ratios.

285

286 Figure S8. Simulated SO_x ($\text{gS}/\text{m}^2/\text{yr}$), NH_x and NO_y ($\text{gN}/\text{m}^2/\text{yr}$) wet deposition for the year
287 2006 compared to EBAS data over Europe. Dashed lines indicate 1:2 and 2:1 ratios.

288

289 Figure S9. Simulated SO_x ($\text{gS}/\text{m}^2/\text{yr}$), NH_x and NO_y ($\text{gN}/\text{m}^2/\text{yr}$) wet deposition for the year
290 2006 compared to EBAS data over Northern America. Dashed lines indicate 1:2 and 2:1
291 ratios.

292

293 Figure S10. Simulated SO_x ($\text{gS}/\text{m}^2/\text{yr}$), NH_x and NO_y ($\text{gN}/\text{m}^2/\text{yr}$) wet deposition for the year
294 2006 compared to EBAS data over Eastern Asia. Dashed lines indicate 1:2 and 2:1 ratios.

295

296 Figure S11. Simulated total aerosol optical depth at 550 nm for the year 2006 compared to the
297 AERONET data worldwide (all available data), over Europe, Northern America, Northern
298 Africa, and Eastern Asia. Dashed lines indicate 1:2 and 2:1 ratios.

299

300 Figure S12. Changes in ammonia surface concentration ($\mu\text{g}/\text{m}^3$) relative to the present-day
301 distribution for scenario RCP8.5 (top) and RCP4.5 (bottom) calculated for 2030 (left) and
302 2100 (right).

303

304 Figure S13. Changes in nitric acid surface concentration ($\mu\text{g}/\text{m}^3$) relative to the present-day
305 distribution for scenario RCP8.5 (top) and RCP4.5 (bottom) calculated for 2030 (left) and
306 2100 (right).

307

308 Figure S14. Changes in sulfate surface concentration ($\mu\text{g}/\text{m}^3$) relative to the present-day
309 distribution for scenario RCP8.5 (top) and RCP4.5 (bottom) calculated for 2030 (left) and
310 2100 (right).

311

312 Figure S15. Changes in nitrate surface concentration ($\mu\text{g}/\text{m}^3$) relative to the present-day
313 distribution for scenario RCP8.5 (top) and RCP4.5 (bottom) calculated for 2030 (left) and
314 2100 (right).

315

316 Figure S16. Changes in nitrate column (mg/m^2) relative to the present-day distribution for
317 scenario RCP8.5 (top) and RCP4.5 (bottom) calculated for 2030 (left) and 2100 (right).

318

319 Figure S17. Evolution of NH_x+NO_y total deposition ($\text{mgN}/\text{m}^2/\text{yr}$) for scenario RCP8.5 (red),
320 RCP6.0 (yellow), RCP4.5 (green) and RCP2.6 (blue) between present-day and 2100. The
321 averaged deposition is depicted for Europe, Northern America, Northern Asia, Southern Asia,
322 India, Africa, Southern America, Australia, the global ocean, and the globe.

323

324 Figure S18. Evolution of the NH_x fractional contribution to NH_x+NO_y total deposition (%) for
325 scenario RCP8.5 (red), RCP6.0 (yellow), RCP4.5 (green) and RCP2.6 (blue) between present-
326 day and 2100. The averaged deposition is depicted for Europe, Northern America, Northern
327 Asia, Southern Asia, India, Africa, Southern America, Australia, the global ocean, and the
328 globe.

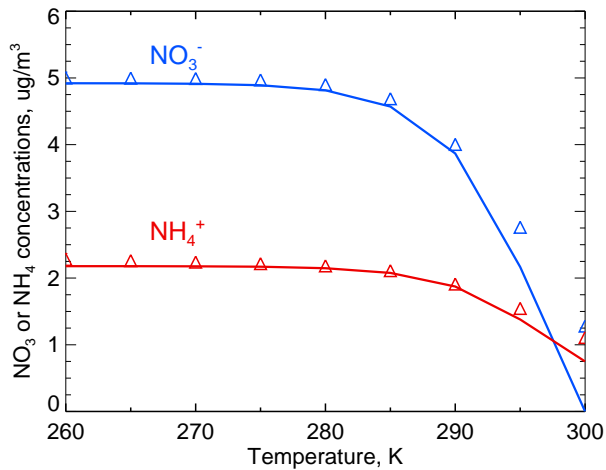
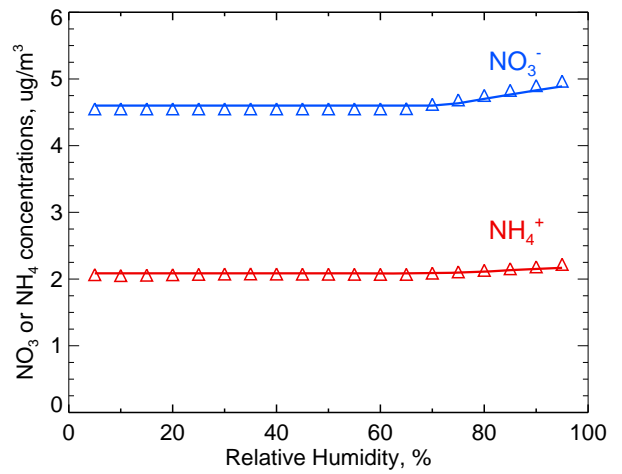
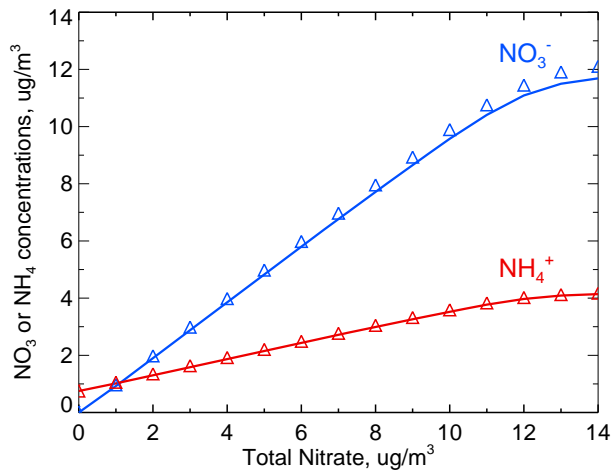
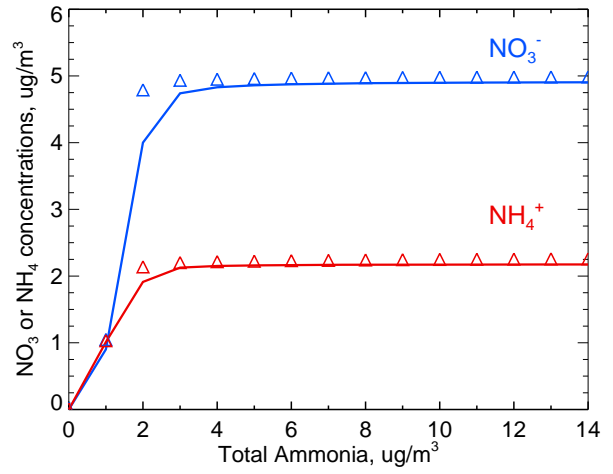
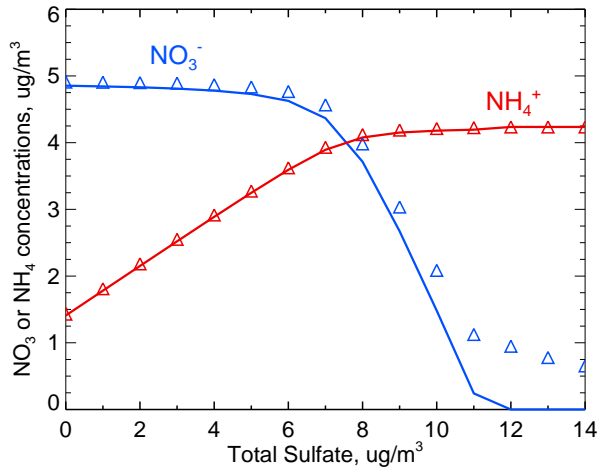


Figure S1

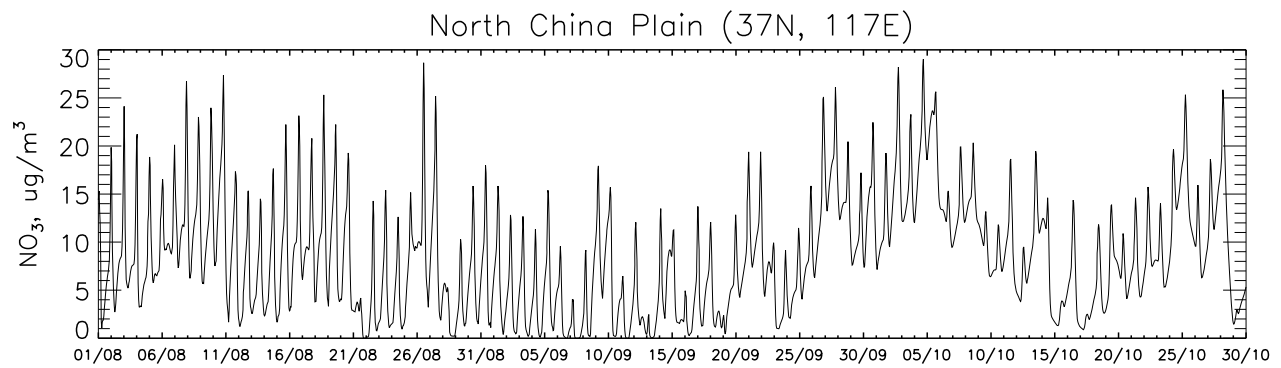
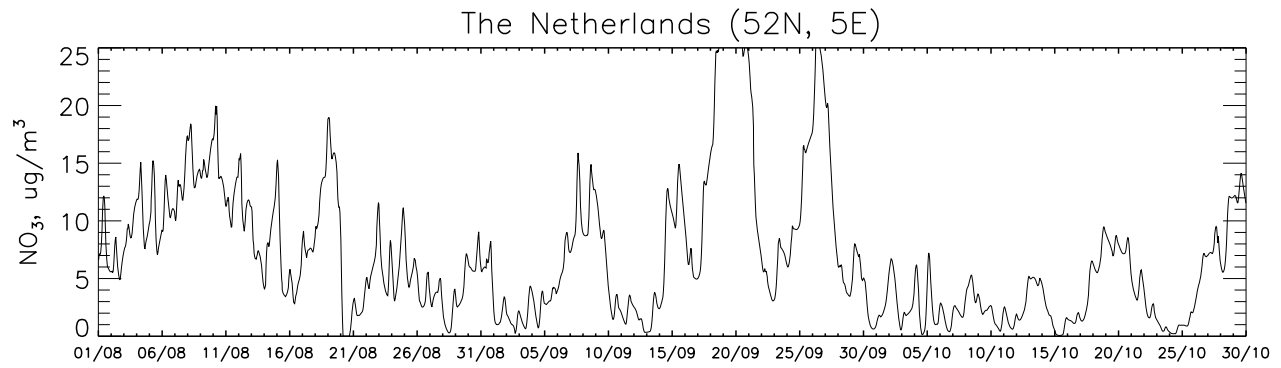
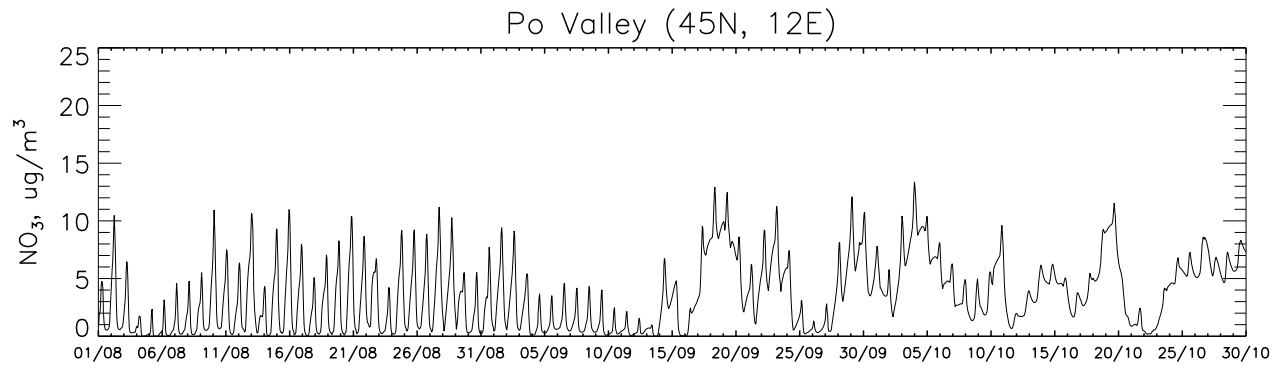
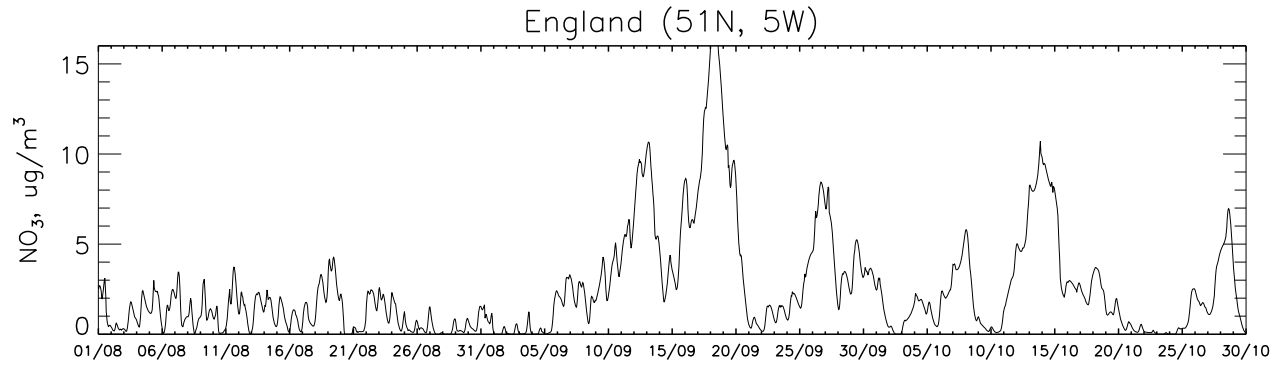


Figure S2

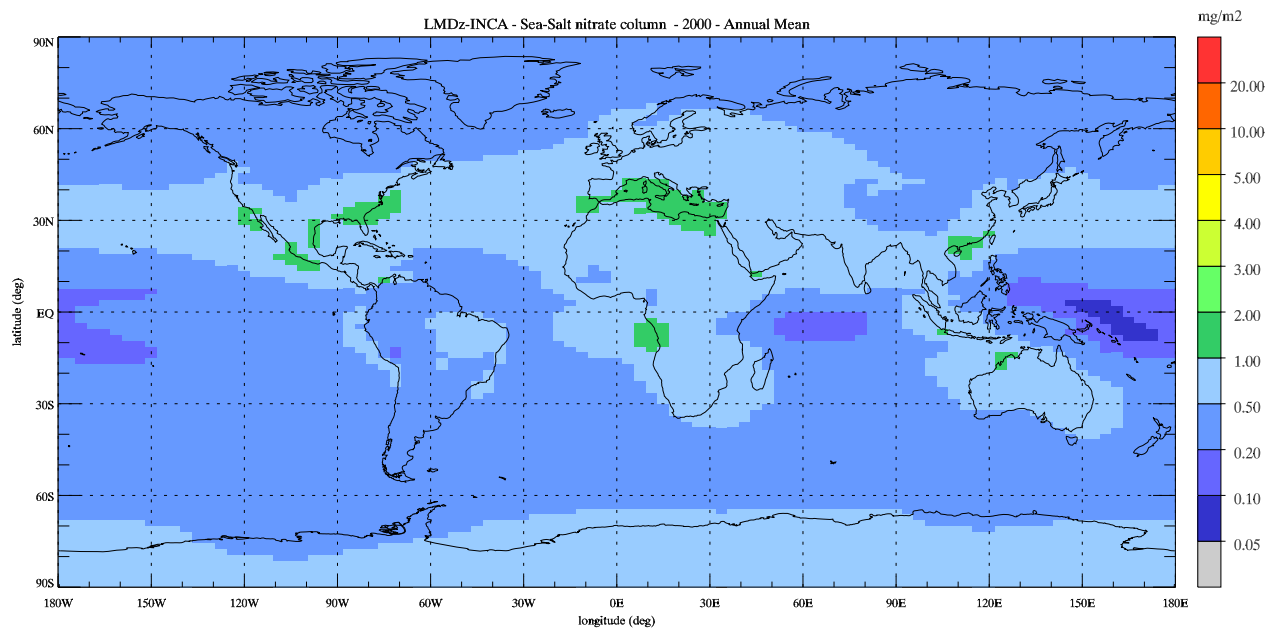
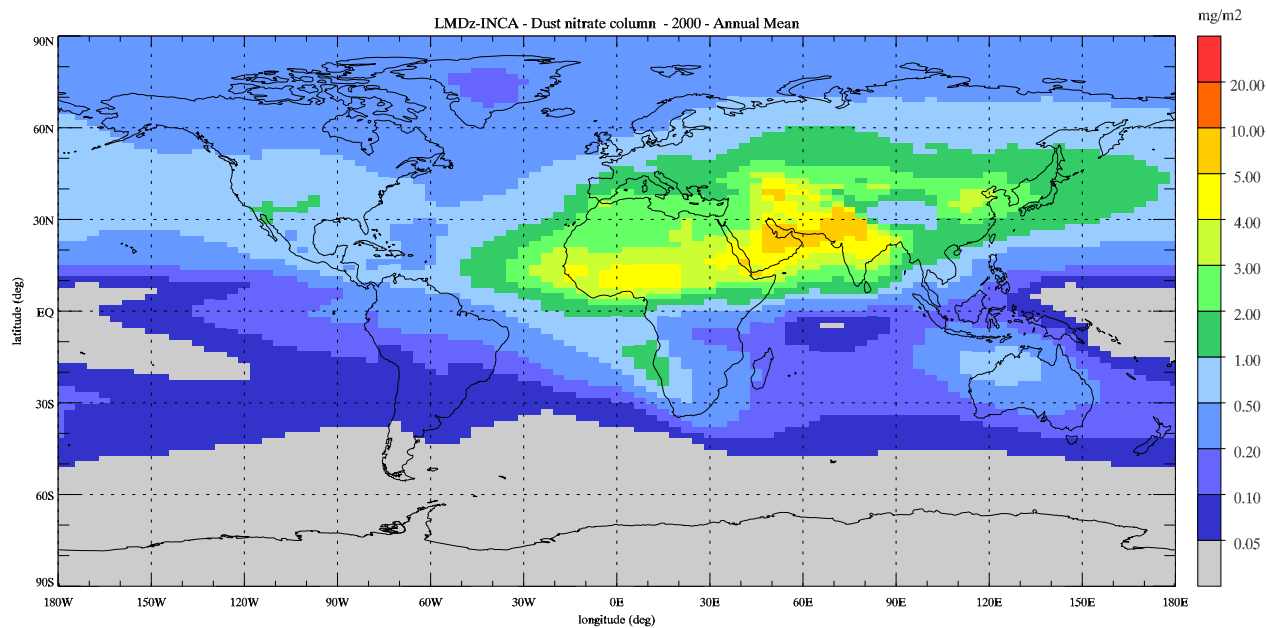
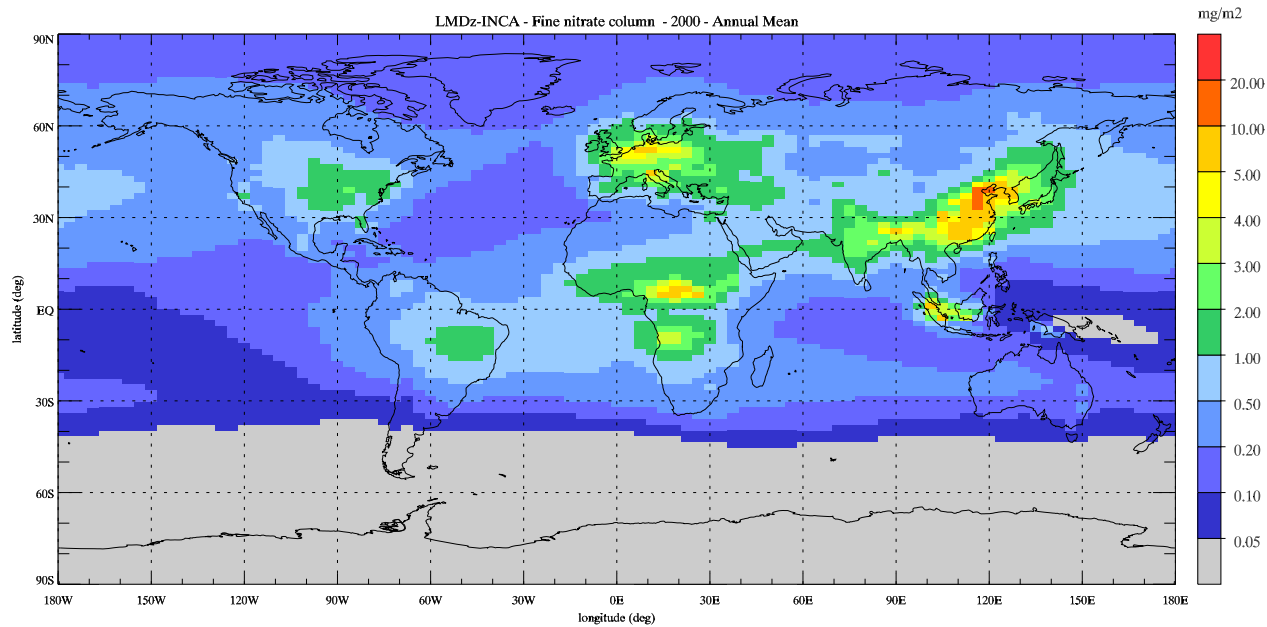


Figure S3

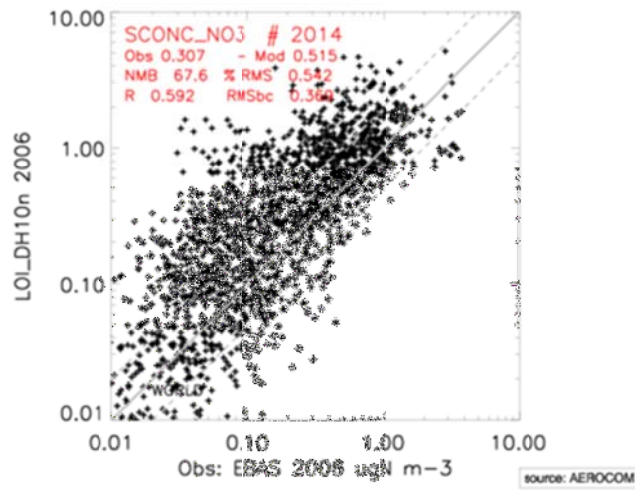
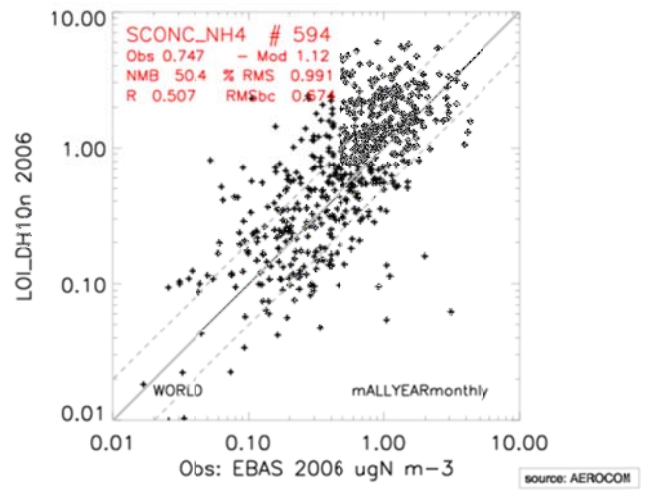
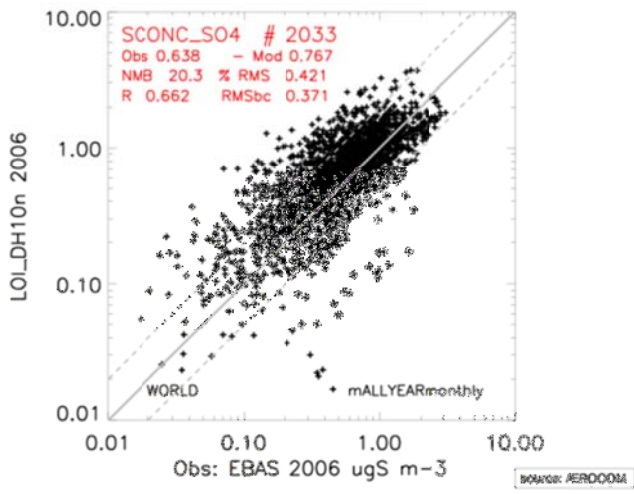


Figure S4

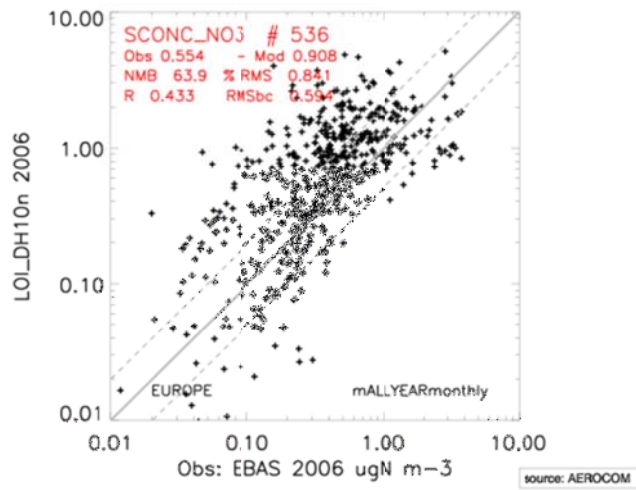
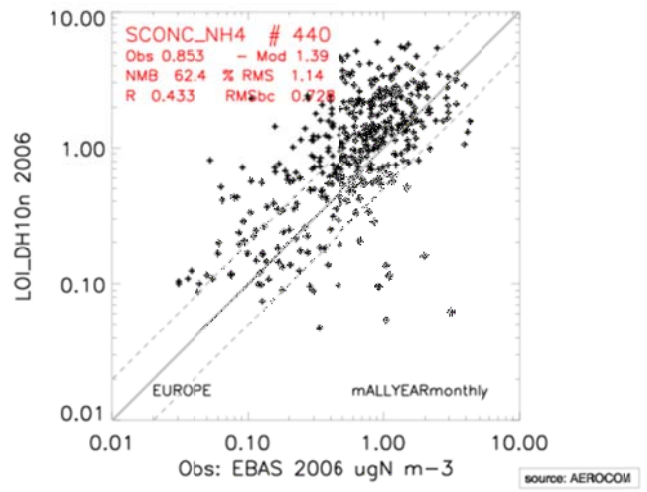
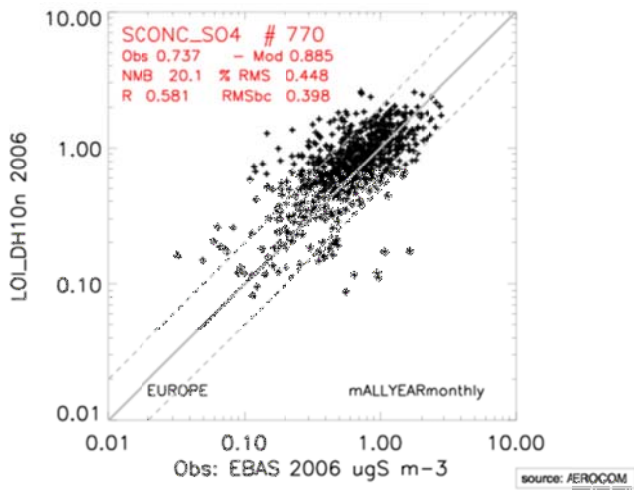


Figure S5

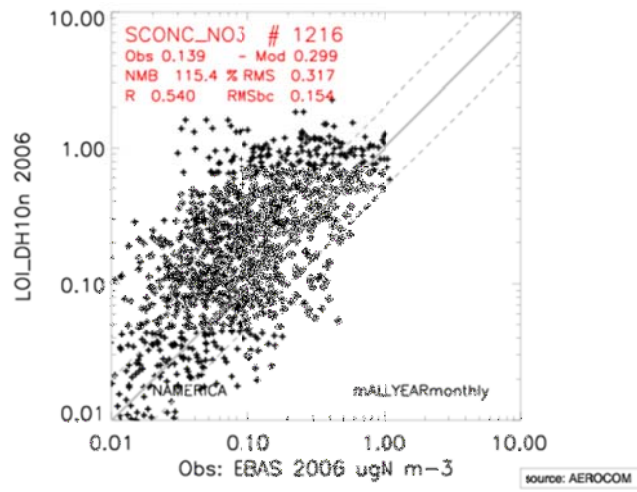
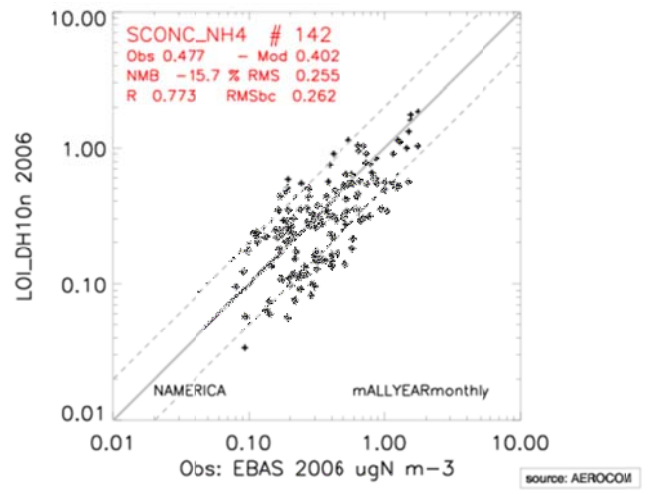
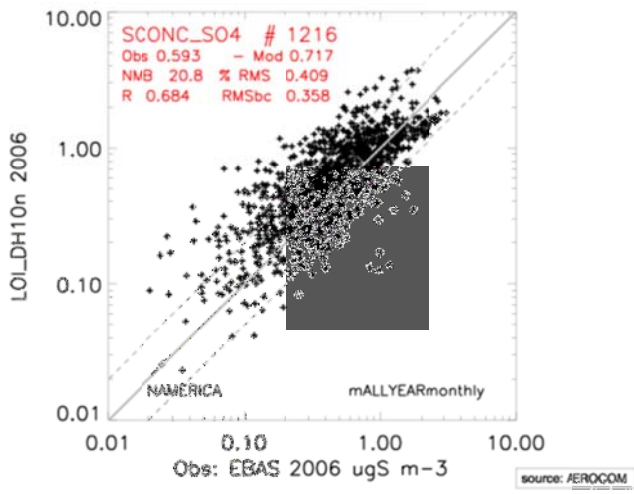


Figure S6

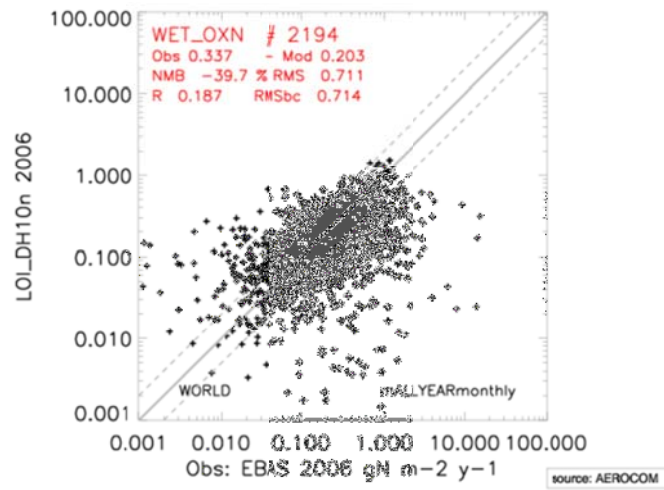
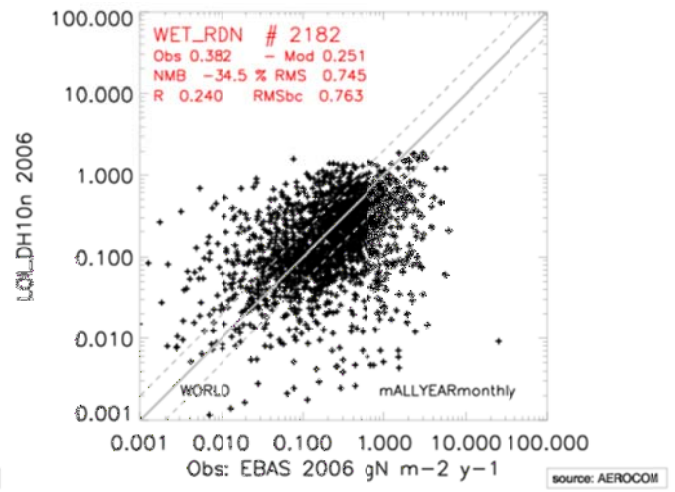
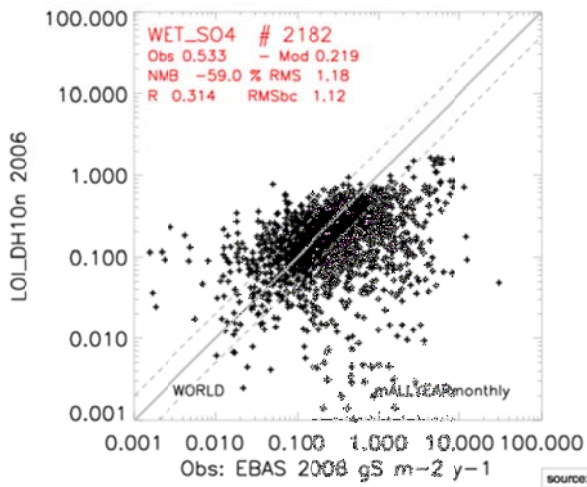


Figure S7

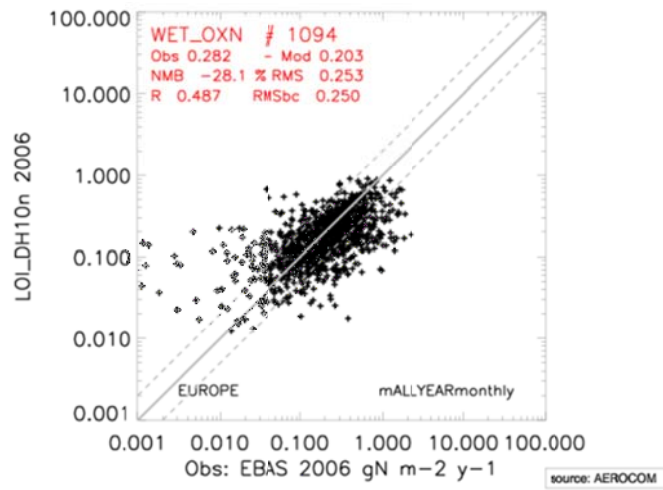
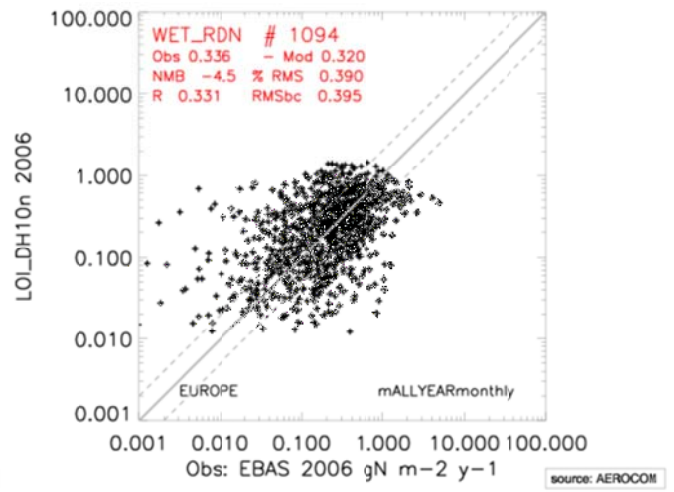
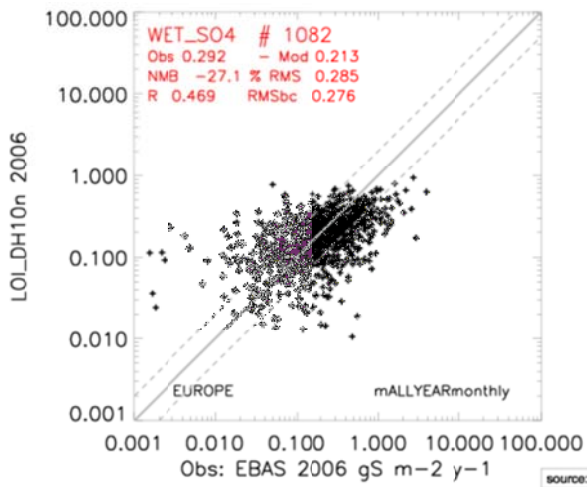


Figure S8

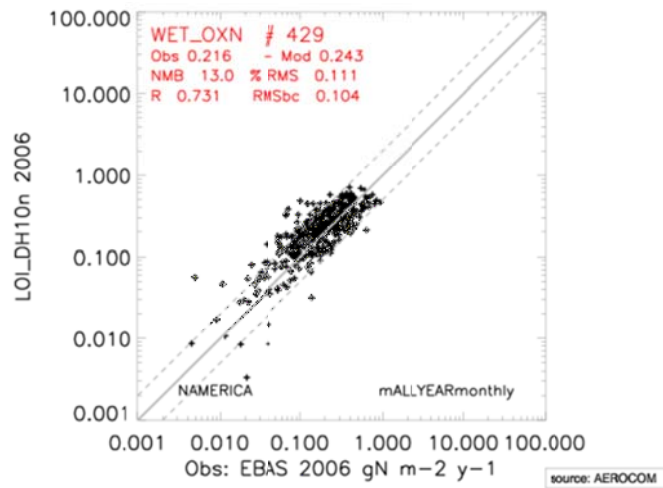
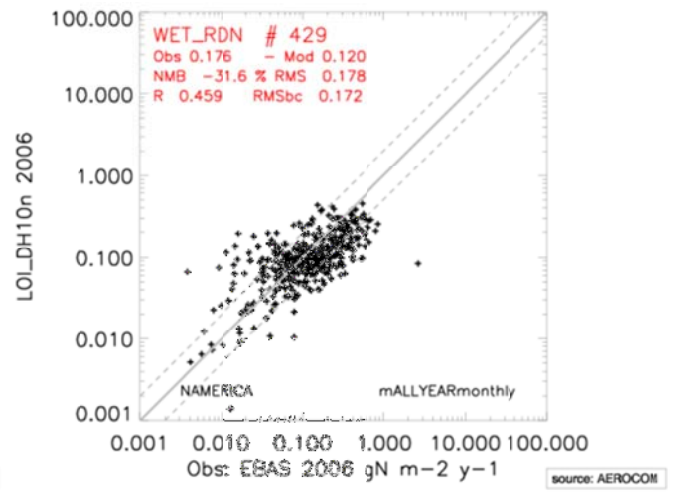
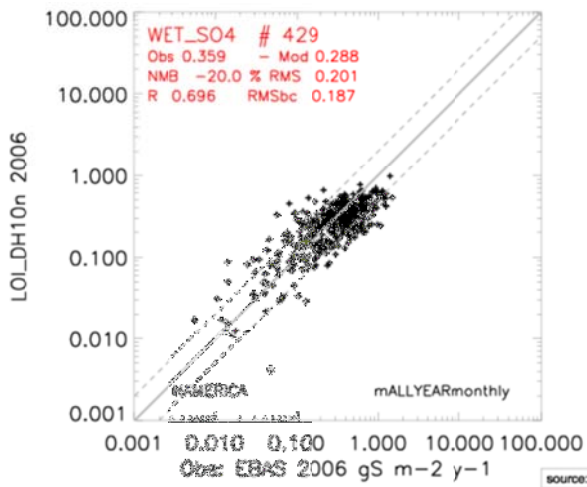


Figure S9

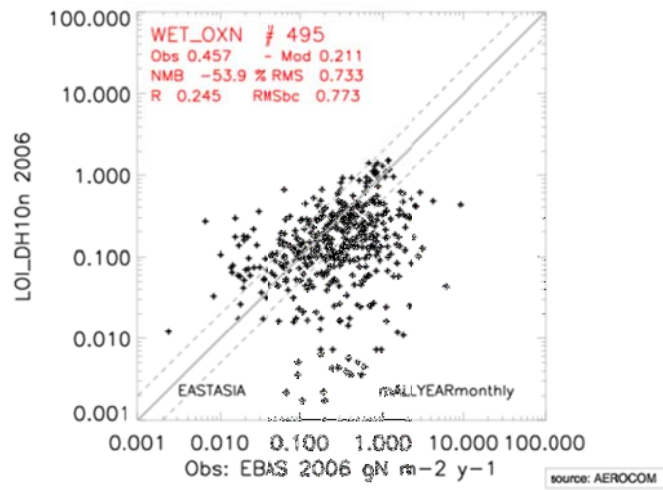
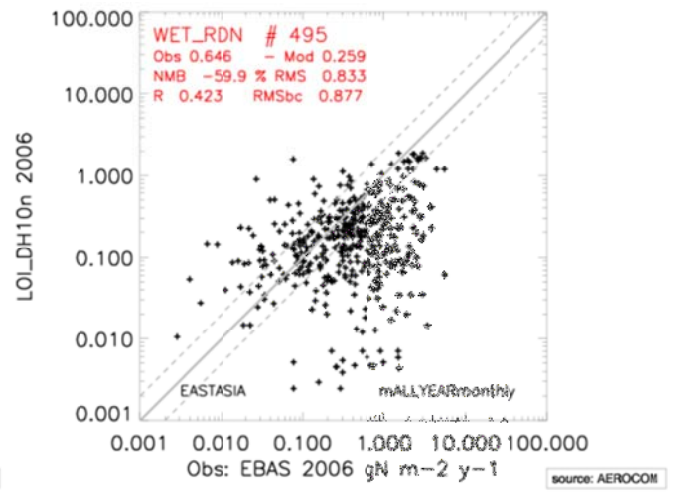
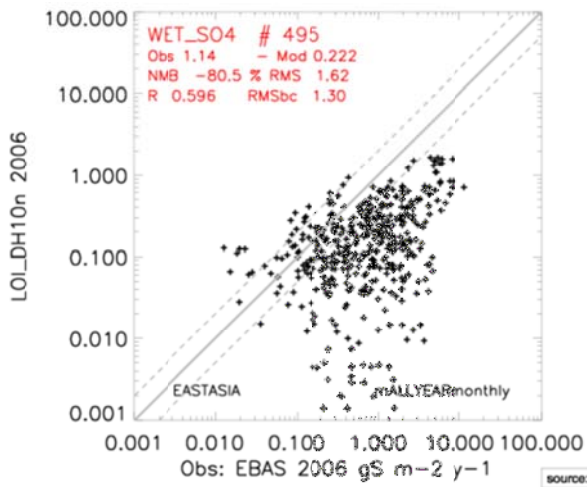


Figure S10

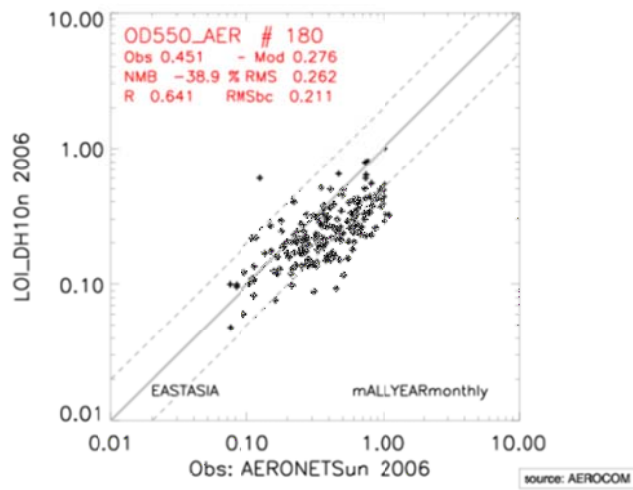
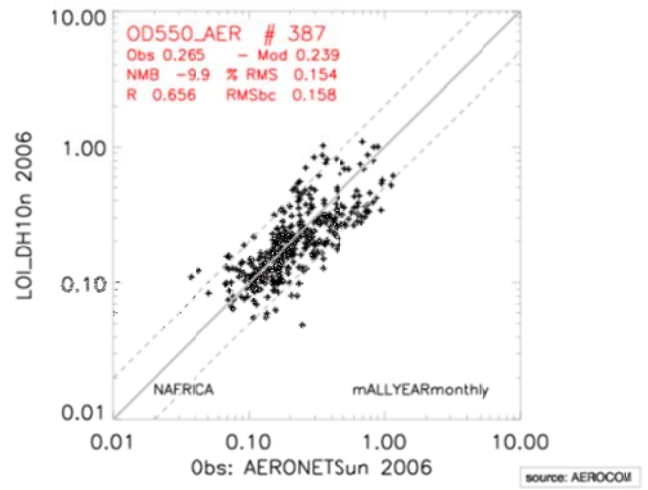
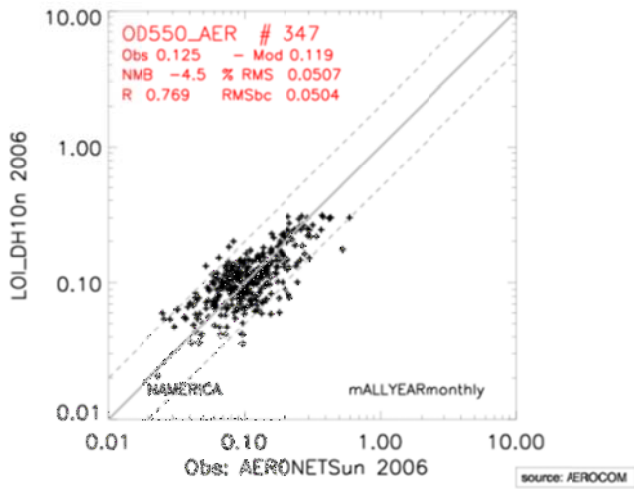
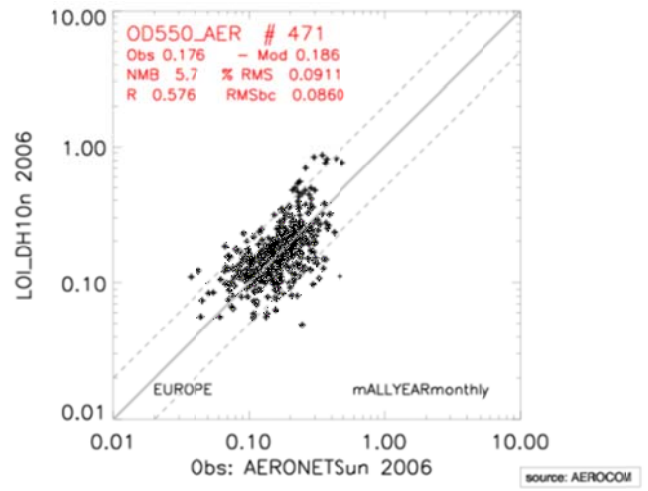
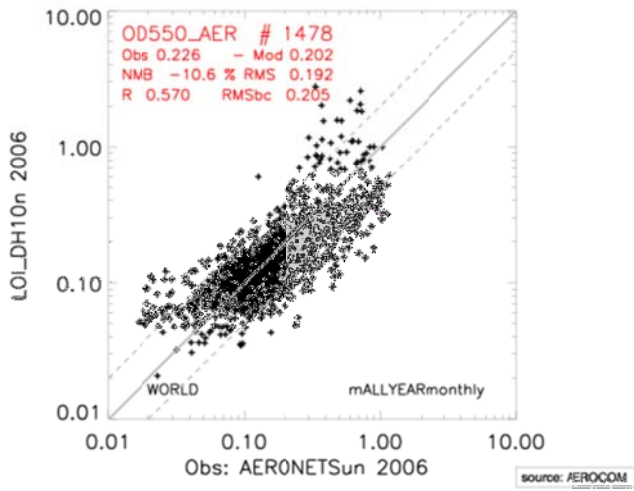


Figure S11

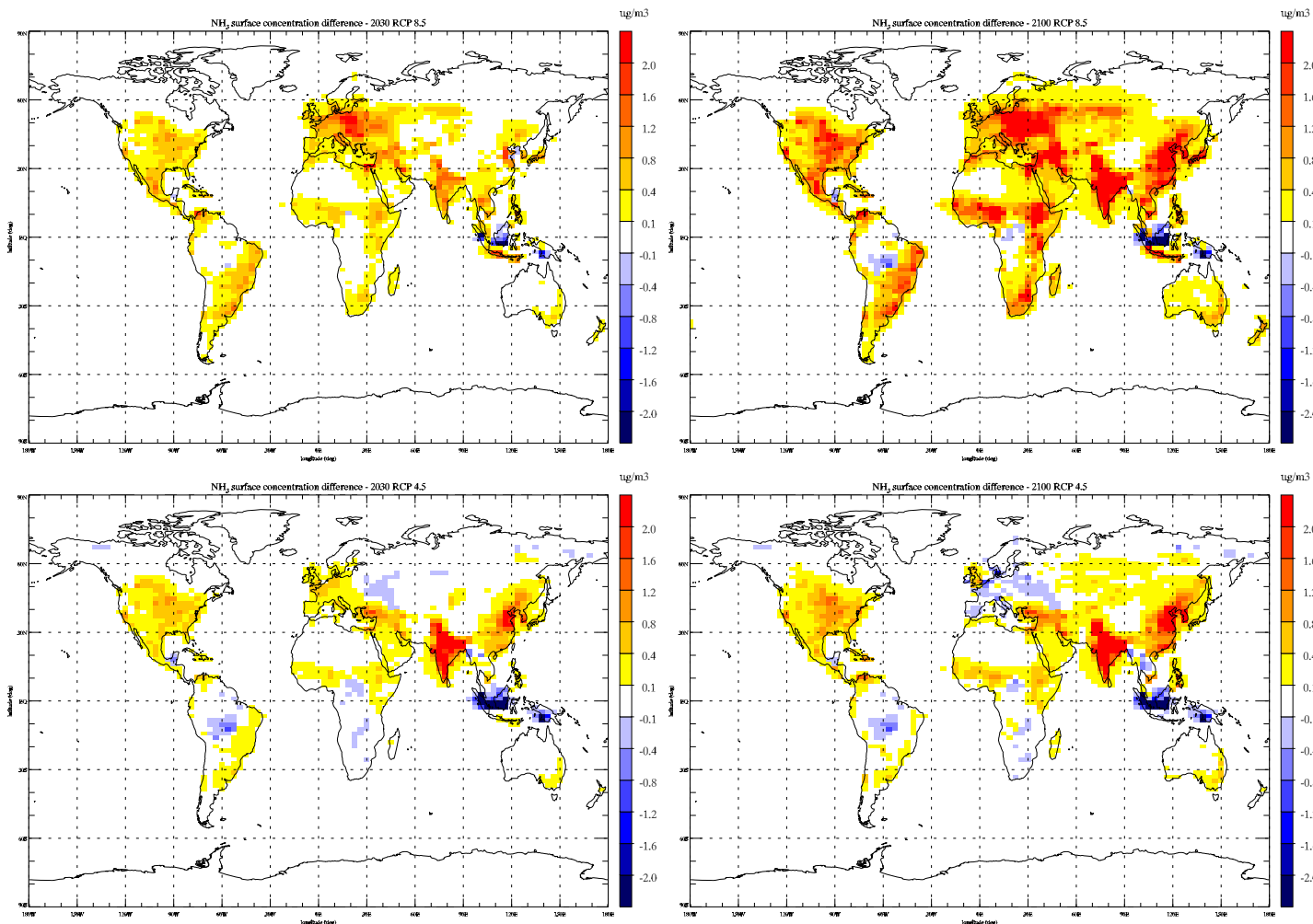


Figure S12

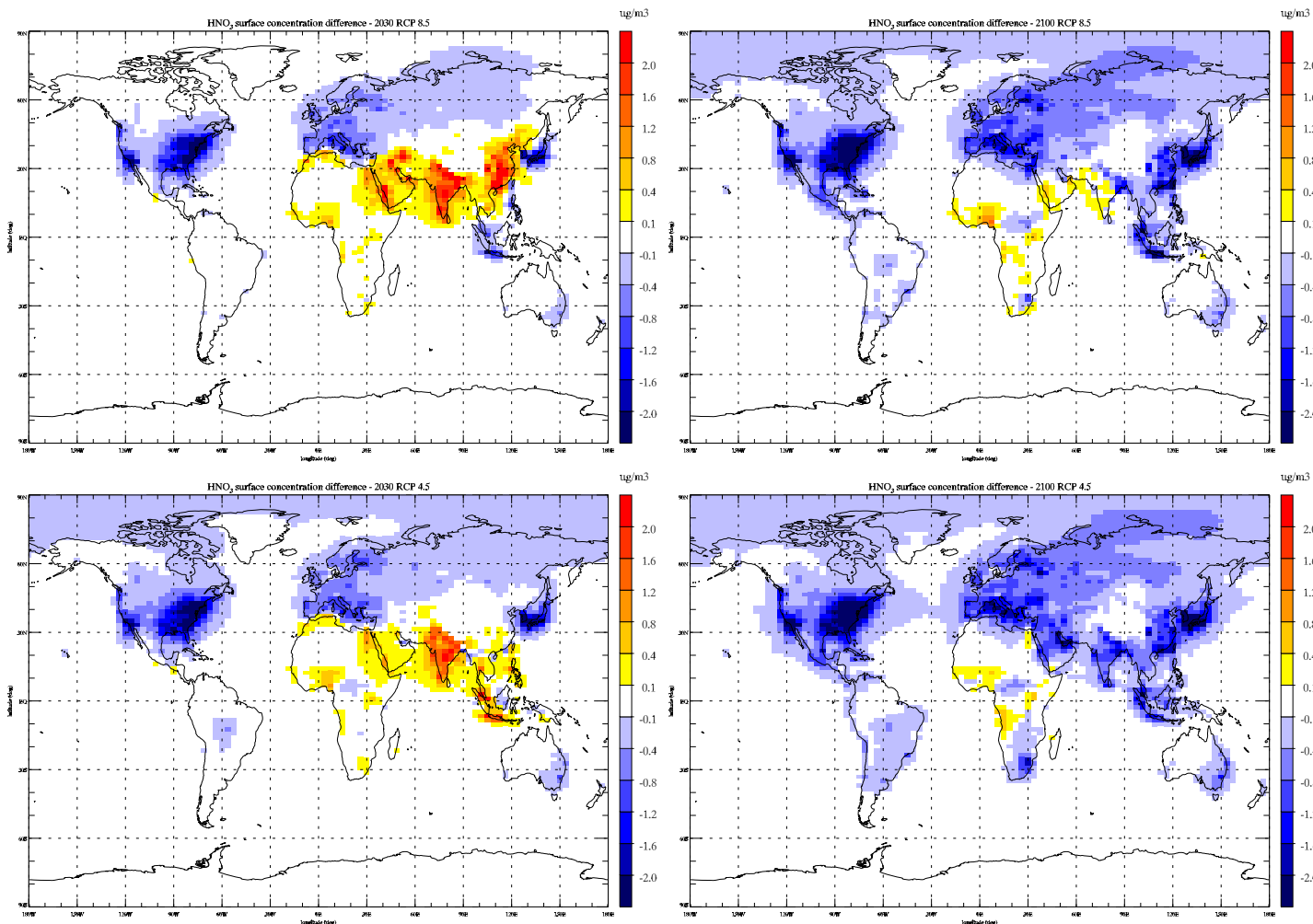


Figure S13

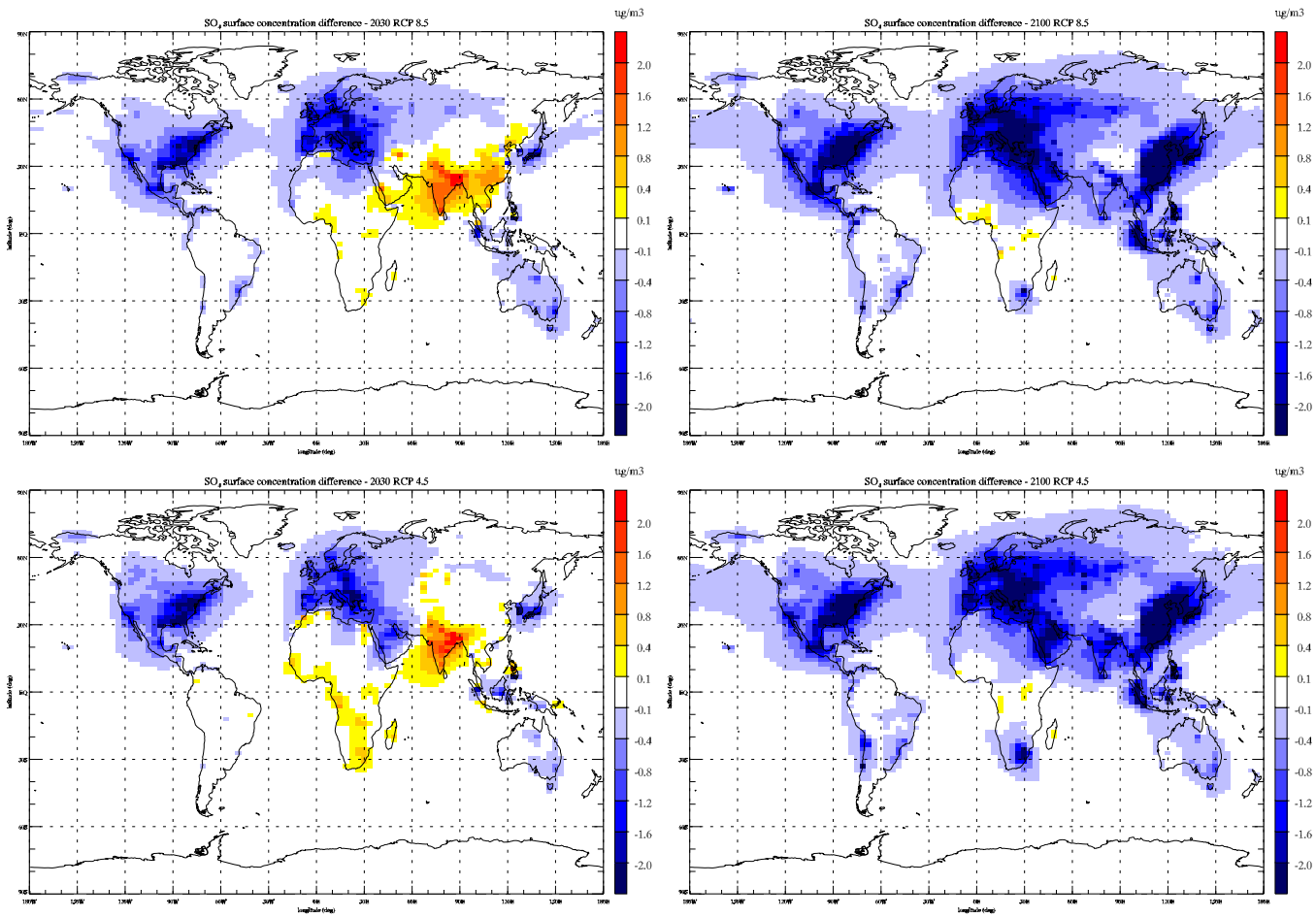


Figure S14

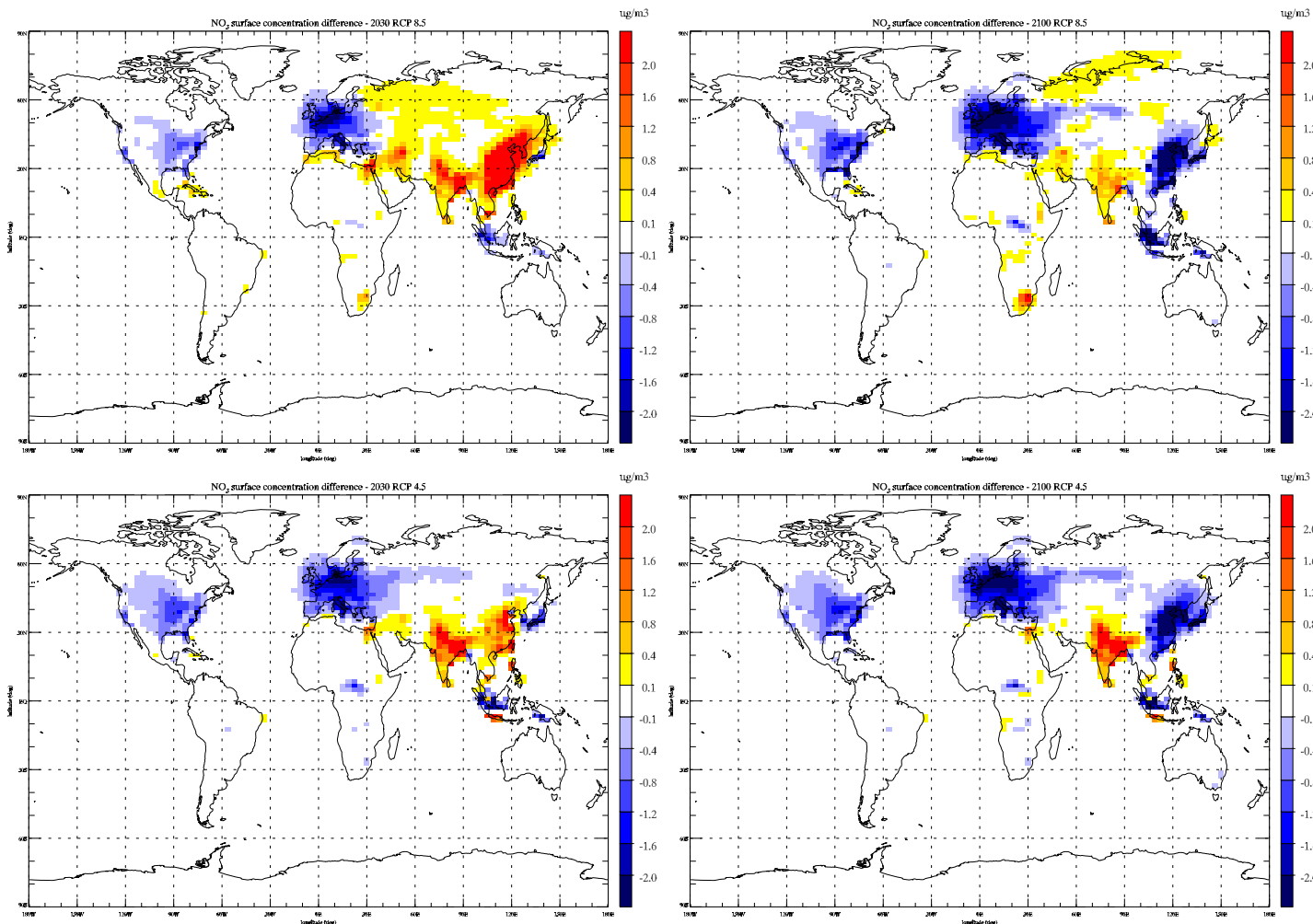


Figure S15

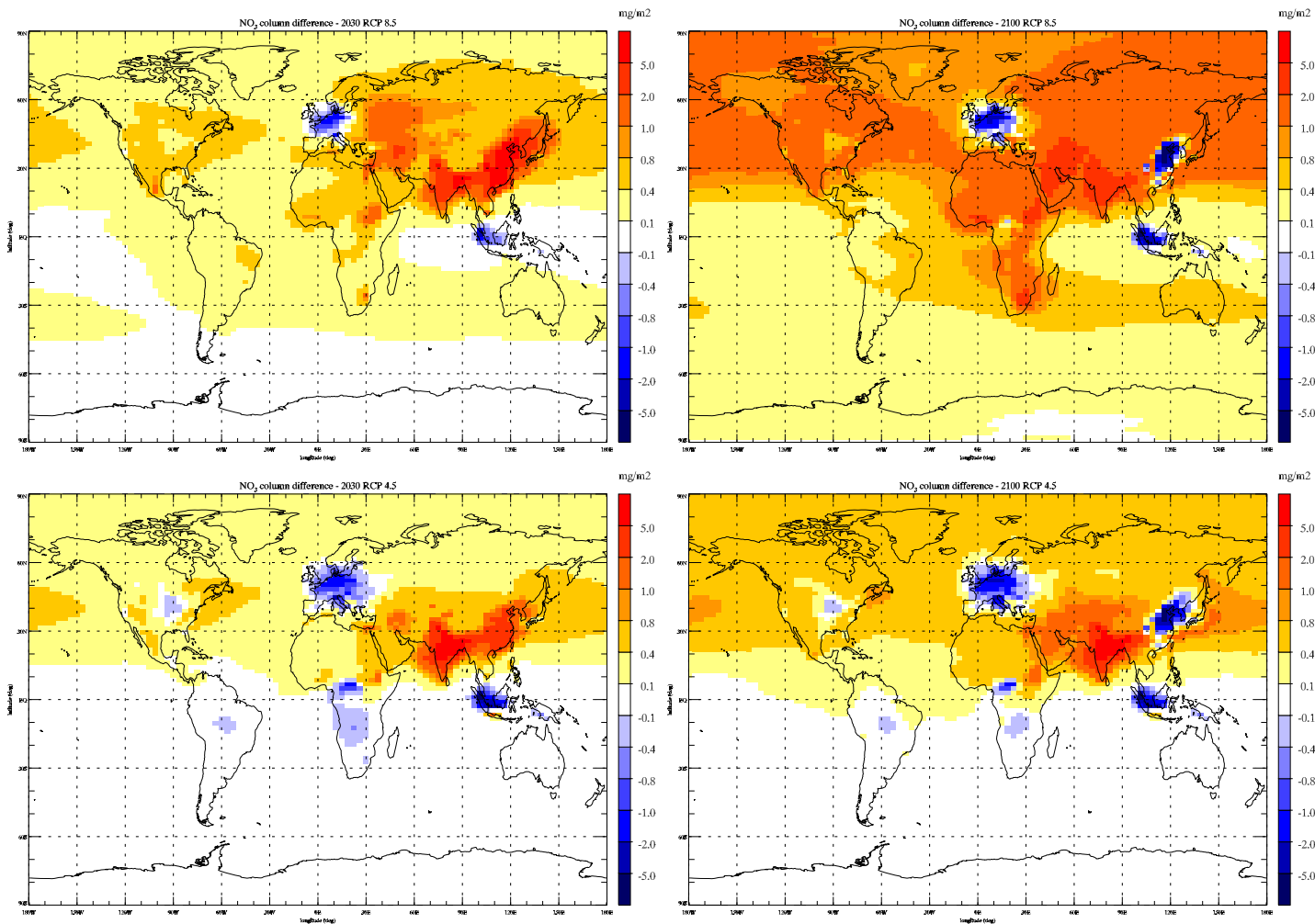


Figure S16

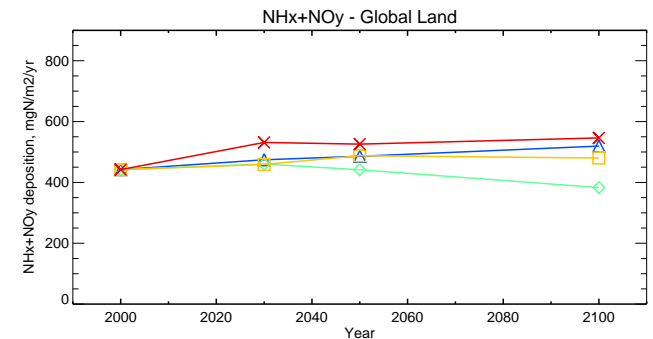
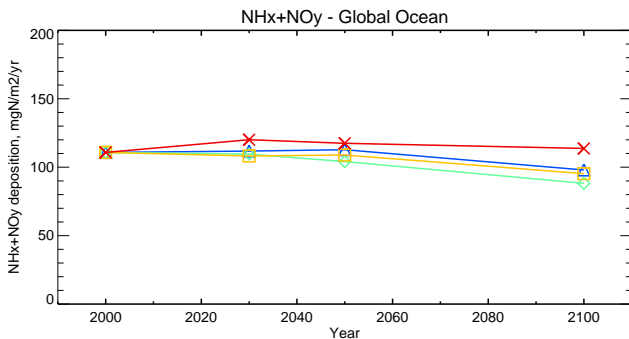
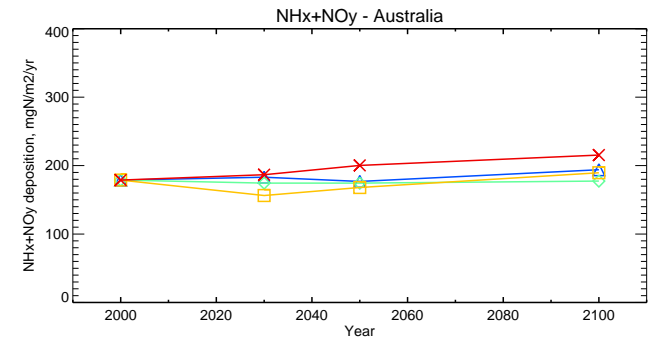
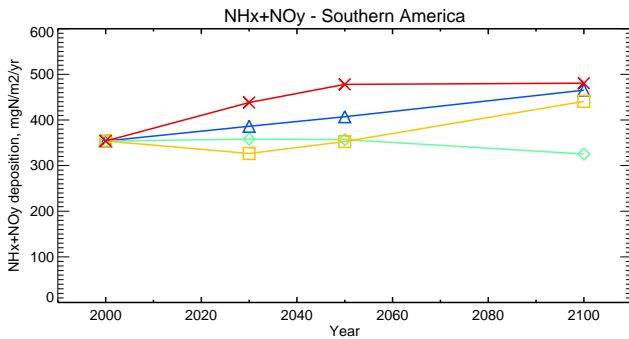
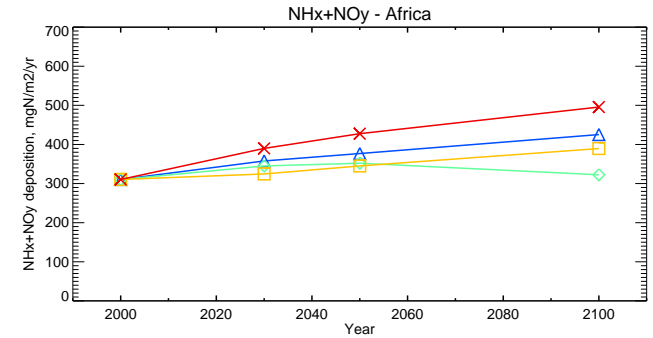
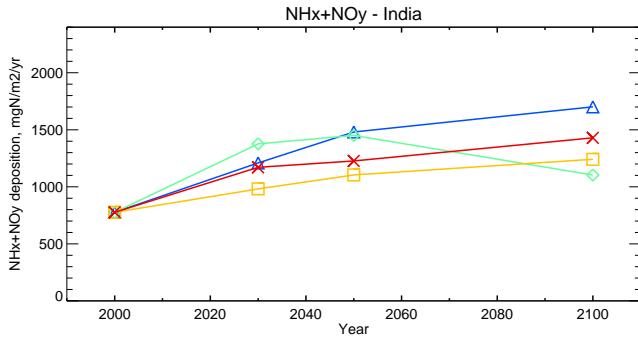
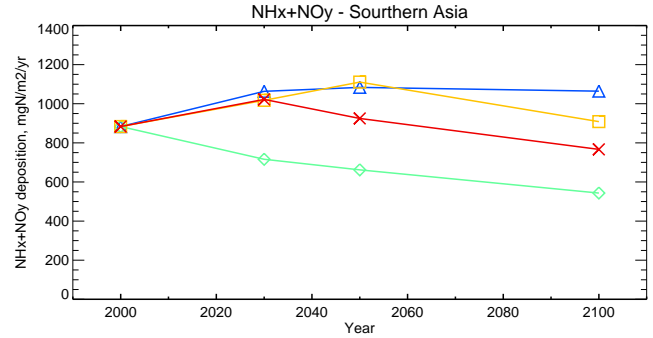
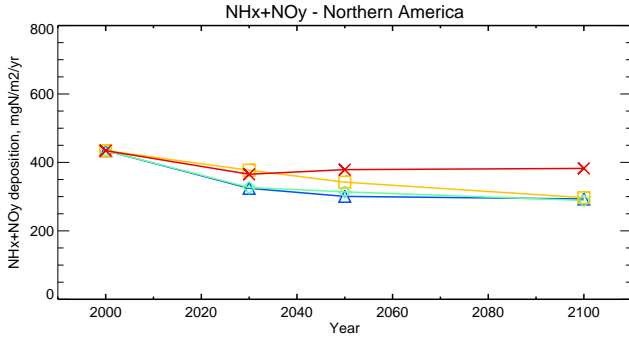
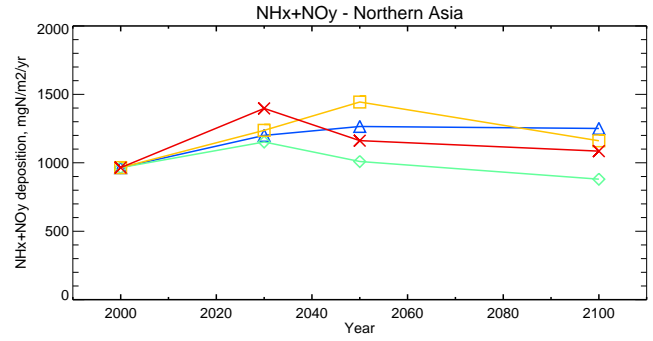
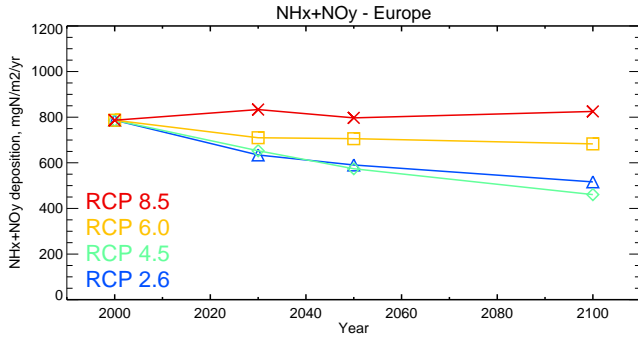


Figure S17

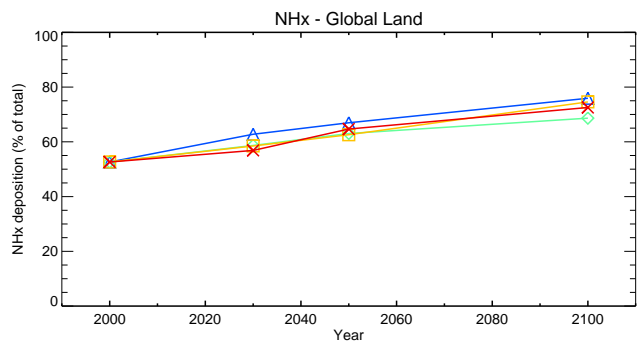
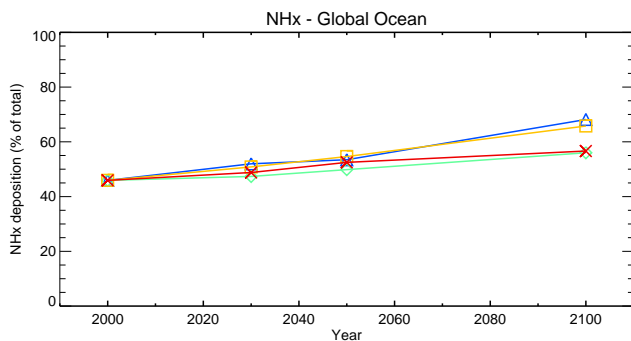
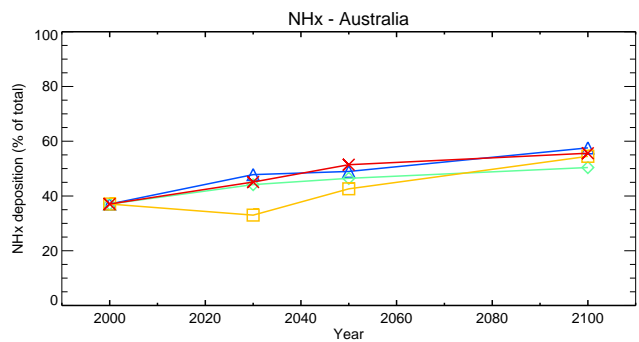
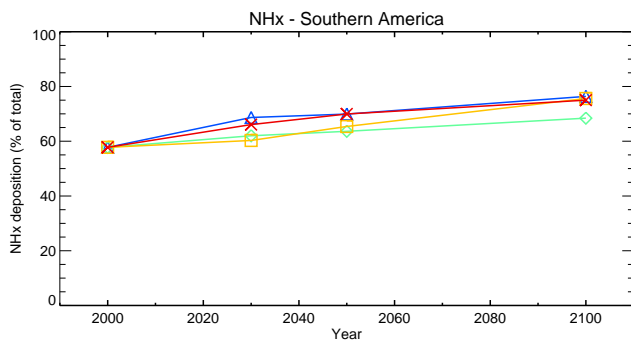
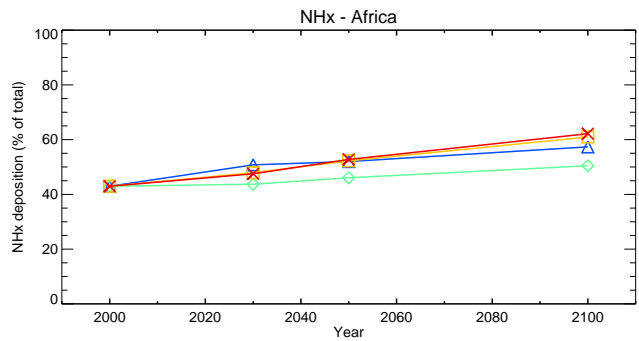
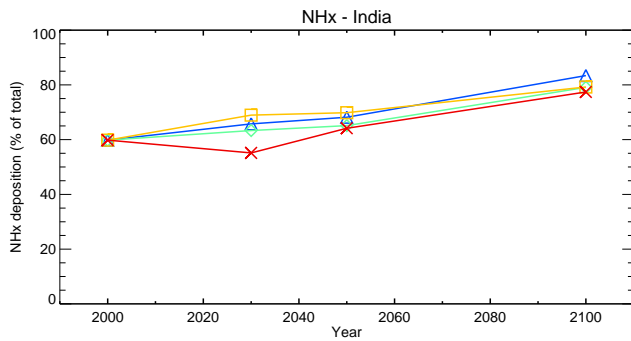
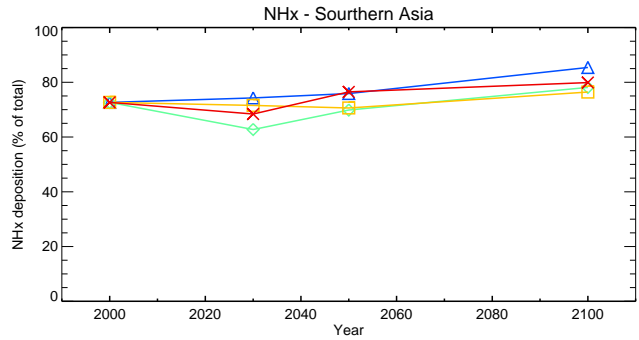
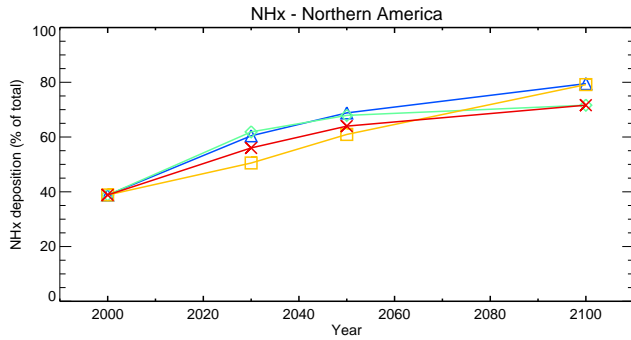
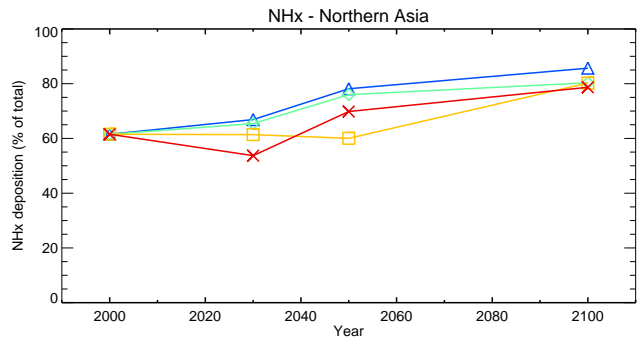
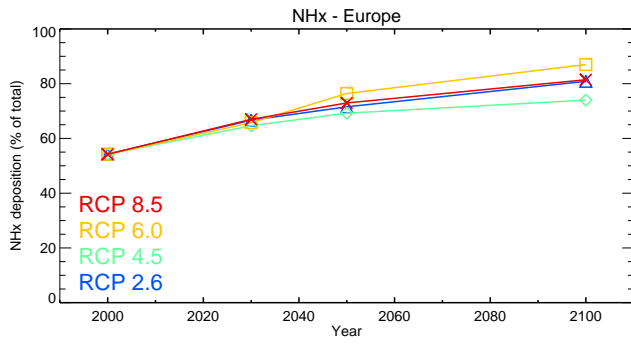


Figure S18